(article starts on next page)

Research on Prediction of Tire Camber-Sideslip Combined Mechanical Characteristics

Yanru Suo[1,2], Dang Lu[1(✉)], Fredrik Bruzelius[2,3], Yandong Zhang[1], and Mattias Hjort[2]

[1] National Key Laboratory of Automotive Chassis Integration and Bionics, Jilin University, Changchun, China
ludang@jlu.edu.cn

[2] Vehicle Systems and Driving Simulation, VTI Swedish National Road and Transport Research Institute, Gothenburg, Sweden

[3] Department of Mechanics and Maritime Sciences, Chalmers University of Technology, Gothenburg, Sweden

Abstract. This article presents a new method to help achieving the rapid response of tire virtual optimization–predicting the camber-sideslip combined mechanical characteristics based on pure camber and pure sideslip. First, the influence mechanism of camber on sideslip is explored. Using the method of combining test and simulation, a finite element (FE) model of 235/55R18 tire is established, and the influence law of camber on sideslip is summarized. Secondly, the prediction method is studied. The linear region prediction is based on the load transferring along tire width caused by camber. The transition zone mechanical characteristics is predicted by treating camber as a function of load and the friction prediction considers local carcass camber (LLC) function. Finally, the application verifications of the prediction method in Magic Formula (MF) and UniTire are carried out. The prediction results are compared with the Similarity result and the MF identification result.

Keywords: Virtual Optimization · Camber · Sideslip · Prediction

1 Introduction

Vehicle virtual prototyping based on simulation technology is an important method to shorten the development cycle of new vehicles, so as to adapt to the automobile market changes driven by electrification and intelligentization [1–3]. Tire virtual optimization aims to allow tires to participate in the early vehicle development process, saving the time and cost caused by the attempts of physical sample tires [4–7]. However, the tire virtual optimization usually uses FE simulation, which has strong nonlinearity [8]. The simulation at combined working conditions can lead to drastic changes in the mesh geometry and aspect ratio, which slows down the simulation speed and even causes convergence problem when using implicit calculation [9].

In view of the current situation, the authors explore the idea of predicting the mechanical characteristics of combined working conditions based on pure working conditions.

This paper focuses on predicting the camber-sideslip combined mechanical characteristics based on pure camber and pure sideslip. Compared with conventional simulation, the prediction method has high precision and effectively saves time and reduces simulation difficulty.

Please note: unless otherwise specified, the text descriptions of the value in this paper all refer to absolute value.

2   The Influence Mechanism of Camber on Sideslip

2.1   Test Result

The Linear Region.   The linear region mechanical characteristics could be represented by cornering stiffness and aligning stiffness. Figure 1 shows the test result of the tire 265/70 R17, which is done by calspan corporation [10]. The cornering stiffness is computed by obtaining the gradient over $\pm 1°$slip angle range. It decreases with the increase of camber angle, while the aligning stiffness shows little change as camber angle varies. Since camber can cause load transfer across the tire width, the linear region characteristics of different loads are displayed, too. The cornering stiffness first increases and then decreases with the load, While the aligning stiffness at different camber angles increases approximately linearly with the load.

(a) Cornering Stiffness (change with camber angle)

(b) Aligning Stiffness (change with camber angle)

(c) Cornering Stiffness (change with load)
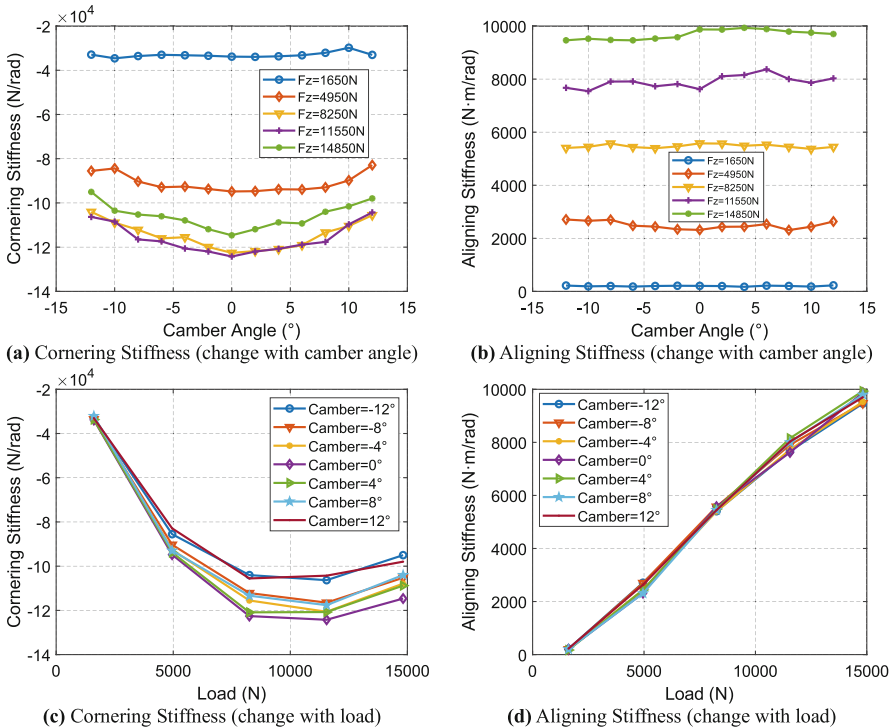
(d) Aligning Stiffness (change with load)

Fig. 1.   Linear region characteristics of the tire 265/70 R17.

The Non-linear Region. The non-linear region could be divided into two zones: the transition zone and the saturation zone. In the transition zone, the tread area is partially slipped, while in the saturation zone, the tread area is fully slipped. As is shown in Fig. 2(a), when camber and sideslip angle have the opposite sign, the lateral force is smaller than that of pure sideslip, and the lateral force reaches its peak later in the transition zone, then decreases slower in the saturation zone, Otherwise the opposite. The influence on aligning torque is different: when camber and sideslip angle have the opposite sign, the aligning torque is bigger than that of pure sideslip, and the aligning torque reaches its peak later in the transition zone, then decreases later in the saturation zone, otherwise the opposite (Fig. 2(b)).
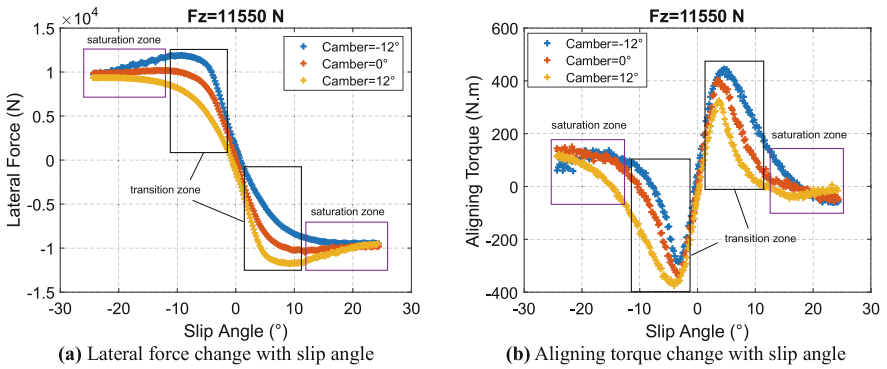
(a) Lateral force change with slip angle   **(b)** Aligning torque change with slip angle

Fig. 2. Non-linear region characteristics of the tire 265/70 R17.

2.2   Mechanism Analysis

To get the carcass deformation and contact patch details for mechanism analysis, an FE model of the tire 235/55 R18 is established (To make it more persuasive to show the proposed prediction method is universal, a different size of tire from the test one is used). The reason of Since the tire FE modeling technology has been mature and considering the article length limit, the modeling details are ignored.

The Linear Region and Transition Zone. Tire carcass lateral deformation is usually divided into three components: the translation deformation (Fig. 3(a)), the bending deformation (Fig. 3(b)) and the Torsion Deformation (Fig. 3(c)). The variables are as follows: y_{c0} represents the translation deformation; F_y the lateral force and k_{cy0}, the translational stiffness. $y_{cb}(x)$ Represents the bending deformation at x position; k_{cb} for the bending stiffness, $\xi(x/a)$ for the bending deformation distribution function and a represents the half length of the contact patch. $y_{\theta x}$ Represents torsional deformation at x position; θ for the torsion angle, $k_{c\theta}$ for the torsional stiffness and M_z represents the aligning torque.

Besides, the camber causes an initial lateral deformation called camber carcass lateral initial deformation (CCLID) [11, 12]. As is shown in Fig. 3(d)), $y_{ini\gamma}(x)$ represents the deformation at x position; γ the camber angle, $y_{\gamma 0}$ the value of $y_{ini\gamma}(x)$ when $x = 0$, and $\varepsilon(x/a)$ is the CCLID distribution function.

(a) Translation Deformation   (b) Bending Deformation   (c) Torsional Deformation   (d) CCLID

Fig. 3. Carcass lateral deformation components.

Figure 4 shows the camber-sideslip combined theoretical model. Where c_α represents the break point of pure sideslip and c represents that of the combined situation. YY_1 represents the tread lateral deformation boundary of the combined situation, while YY_2 represents that of the pure sideslip. YY_3 represents the carcass bending deformation add YY_5, the torsional deformation. YY_4 shows the final carcass position. CCLID is $YY_4 - YY_3$.

Fig. 4. Theoretical model considering carcass lateral deformation.

The lateral force and aligning torque are:

$$F_y = \frac{sign(S_y)\frac{\mu F_z}{2}\int_{-1}^{\sigma_c}\eta(\sigma)d\sigma + a^2 k_{ty}S_y\int_{\sigma_c}^{1}(1-\sigma)d\sigma}{1 + \frac{ak_{ty}}{k_{cb}}\int_{\sigma_c}^{1}\xi(\sigma)d\sigma}$$

$$+ \frac{a^2 k_{ty}\tan\theta\int_{\sigma_c}^{1}(1-\sigma))d\sigma}{1 + \frac{ak_{ty}}{k_{cb}}\int_{\sigma_c}^{1}\xi(\sigma)d\sigma} - \frac{ak_{ty}y_{\gamma 0}\int_{\sigma_c}^{1}\varepsilon(\sigma)d\sigma}{1 + \frac{ak_{ty}}{k_{cb}}\int_{\sigma_c}^{1}\xi(\sigma)d\sigma}$$

(1)

$$M_z = M_{z\gamma}(S_y) + sign(S_y)\frac{a\mu F_z}{2}\int_{-1}^{\sigma_c}\eta(\sigma)\sigma d\sigma$$
$$+ a^3 k_{ty} S_y \int_{\sigma_c}^{1}(1-\sigma)\sigma d\sigma + a^3 k_{ty}\tan\theta\int_{\sigma_c}^{1}\left(\sigma-\sigma^2\right)d\sigma - \frac{a^2 k_{ty}F_y}{k_{cb}}$$
$$\int_{\sigma_c}^{1}\xi(\sigma)\sigma d\sigma - a^2 k_{ty}y_{\gamma 0}\int_{\sigma_c}^{1}\varepsilon(\sigma)\sigma d\sigma \tag{2}$$

where $S_y = -\tan(\alpha)$ with α representing slip angle, $\sigma = x/a$ and k_{ty} represents the tread lateral distribution stiffness. $\sigma_c = x_c/a$, representing the normalization coordinate of break point c. $M_{z\gamma}(S_y)$ shows the aligning torque caused by camber longitudinal distribution force. When $S_y = 0$, the pneumatic trail D is $-a/3$, otherwise:

$$D = \frac{M_z - M_{z\gamma}(S_y)}{sign(S_y)\frac{\mu F_z}{2}\int_{-1}^{\sigma_c}\eta(\sigma)d\sigma + \frac{F_y}{2}\int_{-1}^{\sigma_c}\xi(\sigma)d\sigma + a^2 k_{ty}S_y\int_{\sigma_c}^{1}(1-\sigma)d\sigma + a^2 k_{ty}\tan\theta\int_{\sigma_c}^{1}(1-\sigma)dx} \tag{3}$$

Table 1 shows the parameter values of Eq. (1)–Eq. (3) getting from FE model.

Table 1. Parameter values getting from FE model.

$F_{z(N)}$	$a_{(mm)}$	$k_{ty}(N/m^2)$	$k_{cb(N/m)}$	$k_{c\theta}(Nm/rad)$	$\xi(\sigma)_{(\backslash)}$	$\varepsilon(\sigma)_{(\backslash)}$	$\mu_{(\backslash)}$	$\gamma(°)$	$y_{\gamma 0(mm)}$
1000	38				\				
2000	62								
4000	90								
6000	122	3.89×10^6	6.38×10^6	8.67×10^3	$\frac{3}{2}(1-\sigma^2)$	$1-\sigma^2$	0.8	-6	-3
								0	0
								6	3
7500	148				\				
9000	171								
10000	188								
12000	213								

When $\sigma_c \to -1$, the differential coefficients of Eq. (1) and Eq. (2) are cornering stiffness K_y (Eq. (4)) and aligning stiffness K_m (Eq. (5)). CCLID shows no influence on them.

$$K_y = 2a^2 k_{ty}(1+\frac{K_m}{k_{c\theta}})\bigg/1+\frac{ak_{ty}}{k_{cb}}\int_{-1}^{1}\xi(\sigma)d\sigma \tag{4}$$

$$K_m = -\frac{2}{3}a^3 k_{ty}\bigg/1+\frac{2}{3}a^3\frac{k_{ty}}{k_{c\theta}} \tag{5}$$

The variations of K_y and K_m with load are shown in Fig. 5. Divide the tire into two parts along its width central plane, ideally, these parts are supposed to have the same load-cornering stiffness and load-aligning stiffness curves. Every part works at half load and, contributes half cornering stiffness and aligning stiffness, then we can obtain the half tire results. As is shown in Fig. 5(a), the half tire cornering stiffness at half load F_{zh} is K_{yh}. A camber angle will induce a load shift from one part to the other, causing two half tire loads become F_{zh1} and F_{zh2}, and the corresponding cornering stiffness becomes K_{yh1} and K_{yh2}, respectively. Similarly, the near-linear relationship between aligning stiffness and load causes mild aligning stiffness change with camber.

(a) Cornering Stiffness (change with load)   **(b)** Aligning Stiffness (change with camber angle)
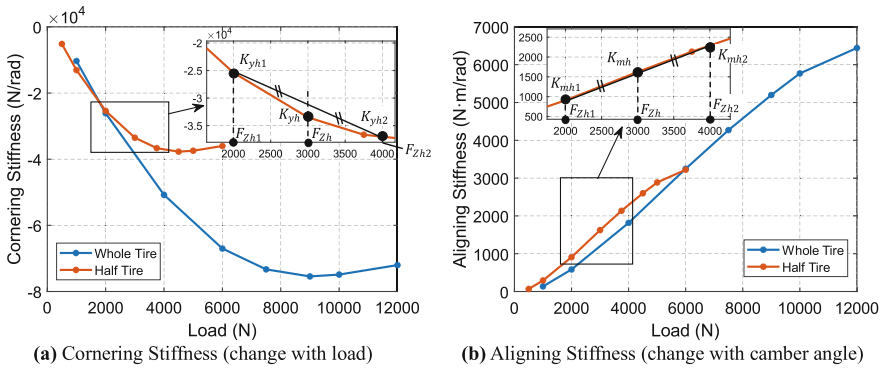
Fig. 5. Theoretical linear region characteristics of sideslip at different loads.

When $-1 < \sigma_c < 1$, the opposite sign camber and slip angle lead to a later break point, then the lateral force is smaller and reaches peak value later (Fig. 6(a)). At the meantime, a bigger and slower-changeable pneumatic trail is obtained, otherwise the opposite (Fig. 6(b)). The lateral force caused aligning torque is shown in Fig. 6(c), that is $M_z - M_{z\gamma}(S_y)$. $M_{z\gamma}(S_y)$ is explained in [11].

Mark $-ak_{ty}y_{\gamma 0}\int_{\sigma_c}^1 \varepsilon(\sigma)d\sigma \Big/ (1 + \frac{ak_{ty}}{k_{cb}}\int_{\sigma_c}^1 \xi(\sigma)d\sigma)$ in   Eq.   (1)   as $\delta_{\gamma F}$, $-a^2 k_{ty}F_y/k_{cb} \cdot \int_{\sigma_c}^1 \xi(\sigma)\sigma d\sigma$ in Eq. (2) as δ_{cbM} and $-a^2 k_{ty}y_{\gamma 0}\int_{\sigma_c}^1 \varepsilon(\sigma)\sigma d\sigma$ in Eq. (2) as $\delta_{\gamma M}$. The lateral force caused by CCLID, $\delta_{\gamma F}$, decreases along the increasing of slip angle, and when the camber and slip angle have the opposite sign, it decreases slower, otherwise the opposite. $\delta_{\gamma M}$ shows the direct aligning torque component caused by CCLID. It increases firstly and then decreases along the increasing of slip angle. When the camber and slip angle have the opposite sign, it changes slower, otherwise the opposite. δ_{cbM} represents the coupling of carcass bending deformation and the CCLID, where the latter has minor influence on F_y. δ_{cbM} has the opposite sign to slip angle, and other laws are the same as $\delta_{\gamma M}$.

The Saturation Zone. Frictional properties determine the saturation zone mechanical characteristics. Friction itself is a highly complex interaction phenomenon between contact materials. The friction characteristics of rubber materials are very complex, which are related to the temperature, humidity, sliding speed and pressure [13]. When the tire is in contact with the road surface, the slip velocity, pressure, and temperature of each
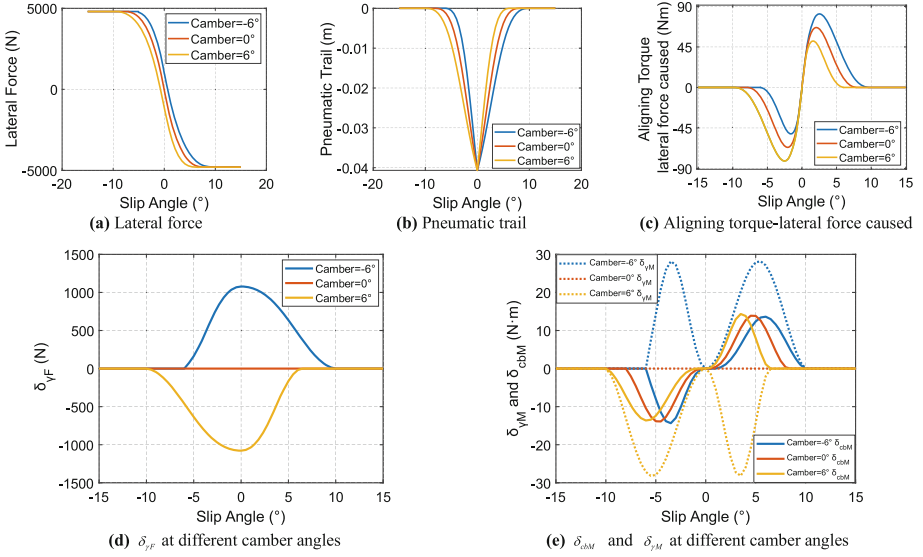
Fig. 6. Camber influence on transition zone.

point in the slip zone of the contact patch are different, and the friction characteristics are more complex. Therefore, the friction of the tire is a comprehensive reflection of the contact surface itself and the contact state between the tire and the road surface.

LCC shows the actual camber angle between the carcass and the road surface [14]. γ is the is the nominal camber angle. When lateral force F_y works on the tire, a lateral movement Δ_{cy} is generated and, a lateral force generated camber angle γ_{cy} happens. So, the LLC angle γ_{ec} could be expressed in Eq. (6):

$$\gamma_{ec} = \gamma_{cy} + \gamma \tag{6}$$

For a cambered tire, γ mainly contributes to the γ_{ec}, γ_{cy} works less. While for a tire with slip angle, γ_{cy} is the only source of γ_{ec}. Three groups of simulations shown in Table 2 are carried out. The result displayed in Fig. 7 shows the equivalence between camber and slip angle. Considering the contact patch load distribution and the contact patch shape, the influence of camber on sideslip friction could be explained by treating camber as a function of slip angle: when the camber and slip angle have the same sign, a smaller equivalent slip angle is generated, then the friction coefficient is bigger, otherwise the opposite.

Table 2. The equivalence between camber and slip angle simulation setting.

Group	Load (N)	Camber Angle (°)	Slip Angle (°)
1	6000	0	−1.4
		3	0
2		0	−2.8
		3	−1.4
3		0	0
		3	1.4

(a) Group 1 load distribution-3D

(b) Group 2 load distribution-3D

(c) Group 3 load distribution-3D

(d) Group 1 load distribution slice-along longitudinal direction

(e) Group 2 load distribution slice- along longitudinal direction

(f) Group 3 load distribution slice- along longitudinal direction

(g) Group 1 contact patch shape

(h) Group 2 contact patch shape

(i) Group 3 contact patch shape

Fig. 7. The equivalence between camber and slip angle considering LLC.

3   Prediction Method

3.1   Cornering Stiffness

Since the aligning stiffness could ignore the influence of camber, only cornering stiffness prediction method is discussed. According to the mechanism analysis in Subsect. 2.2, considering the load shift caused by camber angle, a method of how cornering stiffness changes with camber angle can be obtained as the sum of the cornering stiffness contribution of each part.

Local Load Calculation of Each Part. Local load calculation uses the geometric method. as is shown in Fig. 8, assuming the tire is an isotropic spherical shape, the load acting on the tire is proportional to the deformed volume of the tire. The volume of the undeformed tire intersecting the road surface can represent the deformation of the tire, and the total volume of deformation remains unchanged under different camber angles.
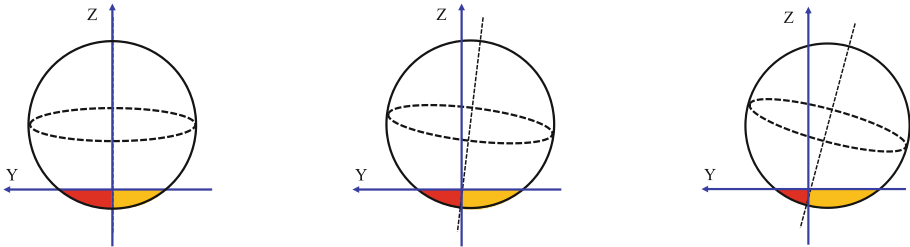
Fig. 8. Load transfer at different camber angles based on "spherical tire" assumption

The actual tire is not spherical, but based on the assumption that the radius of curvature of the tread is equal to the unloaded radius, it is shaped like a part of a sphere, as shown in Fig. 9. Where w is the contact patch width of each part, d is the radial deformation, R_L is the loaded radius. R_y and d_y are the radius and vertical deformation of the plane where the green line is located, respectively. $\theta_y = \arccos(R_L/R_y)$, is half of the central angle corresponding to the contact length of this plane. From the finite element simulation results, it can be seen that if the change of the sharpness of the contact patch shape edge is ignored, the contact patch shape remains unchanged, but the tire surface moves laterally. And the boundary of the tire will limit the shape, "cutting it off". Taking the intersection point of Y axis and R_L as the origin of integration, the load working on every part is calculated as follows:

$$F_{z1} = F_z \frac{\int_{-w}^{-e} (R_0^2 - y^2)\left(\theta_y - \frac{\sin(2\theta_y)}{2}\right)dy}{\int_{-w}^{-e} (R_0^2 - y^2)\left(\theta_y - \frac{\sin(2\theta_y)}{2}\right)dy + \int_{-e}^{w} (R_0^2 - y^2)\left(\theta_y - \frac{\sin(2\theta_y)}{2}\right)dy} \qquad (7)$$

$$F_{z2} = F_z \frac{\int_{-e}^{w} \left(R_0^2 - y^2\right)\left(\theta_y - \frac{\sin(2\theta_y)}{2}\right)dy}{\int_{-w}^{-e} \left(R_0^2 - y^2\right)\left(\theta_y - \frac{\sin(2\theta_y)}{2}\right)dy + \int_{-e}^{w} \left(R_0^2 - y^2\right)\left(\theta_y - \frac{\sin(2\theta_y)}{2}\right)dy} \tag{8}$$

with

$$e = R_L \cdot \tan(\gamma) \tag{9}$$

$$w(x) = \sqrt{R_0^2 - R_L^2}, \, w \le w_0 \tag{10}$$
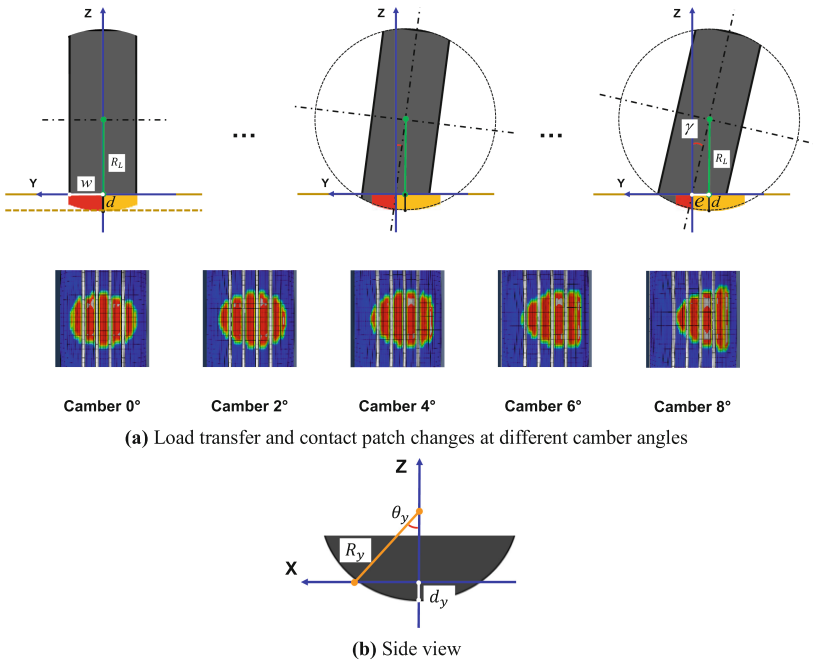
where R_0 is the tire unloaded radius, and w_0 is half the width of the tire.

(a) Load transfer and contact patch changes at different camber angles

(b) Side view

Fig. 9. Diagrammatic view of local load calculation.

Cornering Stiffness of Each Part. From measurements, we can obtain a mapping of how the cornering stiffness is varying as a function of the load for a non-cambered tire. for the complete tire, we have:

$$K_y = f\left(F_z, p_1, p_2 \ldots p_i\right) \tag{11}$$

where $p_1, p_2 \ldots p_i$ are model parameters. Then for a half tire, we have:

$$\frac{K_y}{2} = f\left(\frac{F_z}{2}, p_1', p_2' \ldots p_i'\right) \tag{12}$$

where model parameters are updated to $p_1', p_2' \ldots p_i'$. For MF and UniTire model [15], the half tire cornering stiffness is described in Eq. (13) and Eq. (14), respectively.

$$K_{yiMF} = \frac{p_1}{2} \cdot \sin\left(2\arctan\left(\frac{F_{zi}}{p_2/2}\right)\right), i = 1, 2 \tag{13}$$

$$K_{yiUniTire} = s_{11}\mathrm{sech}\left(2^2 s_{12}F_{zn}^2 + 2s_{13}F_{zn}\right), i = 1, 2 \tag{14}$$

3.2 Transition Zone

Lateral force shown in Fig. 4 could be replaced by the sum of Fig. 10(a) and Fig. 10(b). Figure 10(a) could be treated as the sideslip lateral force considering camber influence. The biggest lateral force of boundary YY_2 could generate is $\mu F_z / (2a) \cdot \eta(\sigma)$, while that of boundary YY_1 is $\mu F_z / (2a) \cdot \eta(\sigma) + sign(\alpha)3F_{y\gamma} / (4a) \cdot \varepsilon(\sigma)$, marked as $F_{y_{\alpha\gamma}}$, where $F_{y\gamma}$ represents the camber thrust. When the $\eta(\sigma)$ and $\varepsilon(\sigma)$ are both in parabolic form, we have:

$$F_{y_{\alpha\gamma}} = \mu / 2a \cdot \eta(\sigma)\left(F_z + sign(\alpha)F_{y\gamma} / \mu\right) \tag{15}$$

Mark $F_{ze} = F_z + sign(\alpha)F_{y\gamma} / \mu$, representing the equivalent load considering camber influence. Then the camber-sideslip combined lateral force could be expressed in:

$$F_y = F_{y_{\alpha\gamma}} + F_{y\gamma} \tag{16}$$

Calculating $F_{y_{\alpha\gamma}}$ by replacing the test load F_z in pure sideslip by F_{ze}. The similar for the pneumatic trail prediction. In this way, the combined lateral force and the lateral force caused aligning torque could be obtained.

The conicity is caused by the deviation of the belt layer from the tire geometric center during the manufacturing process, or the camber of the belt itself. Its function is similar as camber and is the aligning torque source for the free rolling tire. By parameterizing the pure sideslip test data, the conicity aligning torque change law with slip angle $\lambda_{Mz\gamma}$ could be obtained. Considering the similarity of conicity and camber, this $\lambda_{Mz\gamma}$ is used for the calculation of $M_{z\gamma}(S_y)$. Then the whole aligning torque is obtained.

3.3 Friction

The empirical formula shown in Eq. (17) is used to express the influence of velocity on the friction coefficient during pure sideslip, where $\mu_0(F_z)$ is the static friction affected by the load, and $\Delta\mu(v_{sy})$ is the difference between the dynamic and static friction affected by the tire lateral slip velocity v_{sy}.

$$\mu_d = \mu_0(F_z) - \Delta\mu(v_{sy}) \tag{17}$$

When considering LLC, Eq. (18) is changed to:

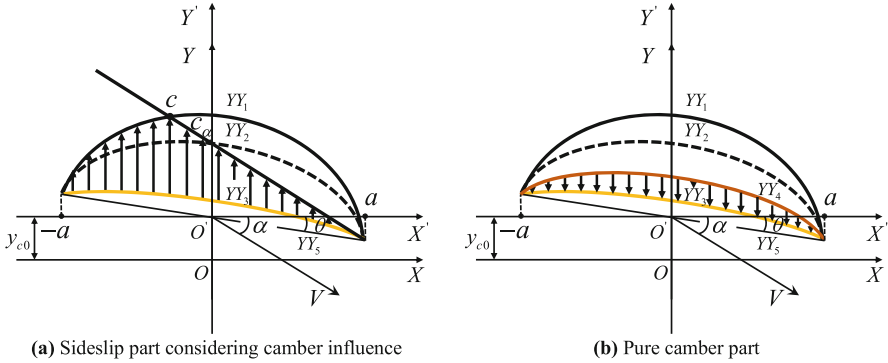$$\mu_d = \mu_0(F_z, LLC) - \Delta\mu(v_{sy}) \tag{18}$$

(a) Sideslip part considering camber influence   (b) Pure camber part

Fig. 10. Transition zone prediction diagrammatic drawing.

For pure sideslip, mark *LLC* as LLC_α, representing the LLC caused by slip angle:

$$LLC_\alpha = F_y / K_L \qquad (19)$$

where K_L is the tire lateral translational stiffness. As is shown in Fig. 11(a), LLC_α promotes the load distribution uneven, so the μ_0 is supposed to decrease with the increase of LLC_α. When ignoring this function, we get the constant LLC_α curves. The intersections of these curves and the corresponding slip velocity shows the changed LLC_α result, that is, the pure sideslip friction (Fig. 11(a)). For camber-sideslip combined situation, similar result is shown in Fig. 11(b), respectively, with:

$$LLC = LLC_\alpha + \gamma \qquad (20)$$

By treating camber as an equivalent slip angle $\Delta\alpha$, the combined friction could be predicted by pure sideslip and pure camber. The LLC_α and sideslip velocity influence are coupled in sideslip test, so $\Delta\mu$ is supposed to represent their whole influence. The $\Delta\alpha$ is put into the $\Delta\mu$ function in Eq. (21):

$$\mu_d = \mu_0(F_z) - \Delta\mu(\alpha + \Delta\alpha_f) \qquad (21)$$

where $\Delta\alpha_f = F_{y\gamma} / K_L$. The prediction result is shown in Fig. 11(c).

(a) Pure sideslip friction   (b) Combined friction (negative camber)   (c) Predicted friction (negative camber)
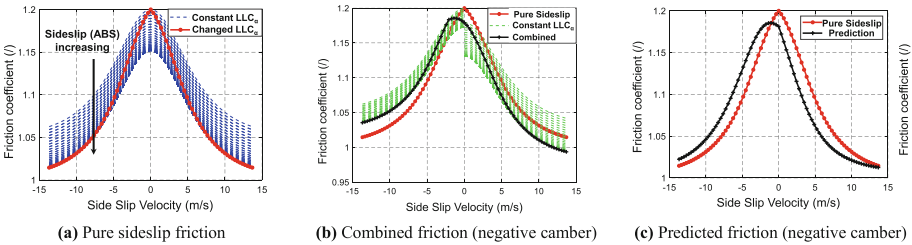
Fig. 11. Friction prediction.

4 Application Verification

The method is supposed to be universal and is applied in MF and UniTire model. Based on the size of 265/70R17 tire test results, the prediction result of MF model is compared with the Similarity method and the MF identification results. As is shown in Fig. 12, the prediction application in MF obtains a better cornering stiffness result than Similarity got, and has high overall accuracy. The UniTire result is compared with the MF identification effect. The result in Fig. 13 shows high accuracy, which can be used as a new way to obtain the mechanical characteristics of combined working conditions.
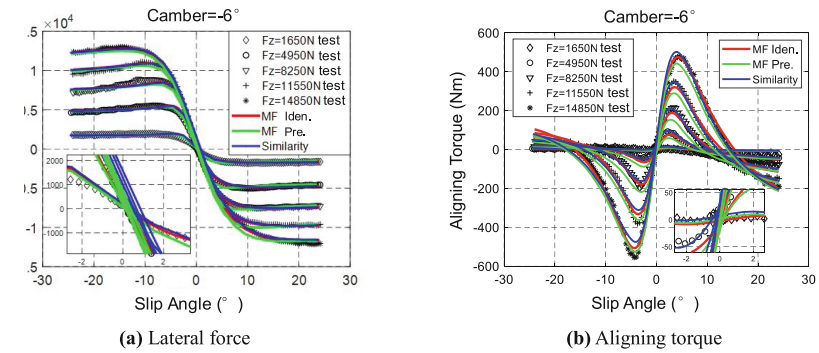

(a) Lateral force   (b) Aligning torque

Fig. 12. Prediction result of MF.

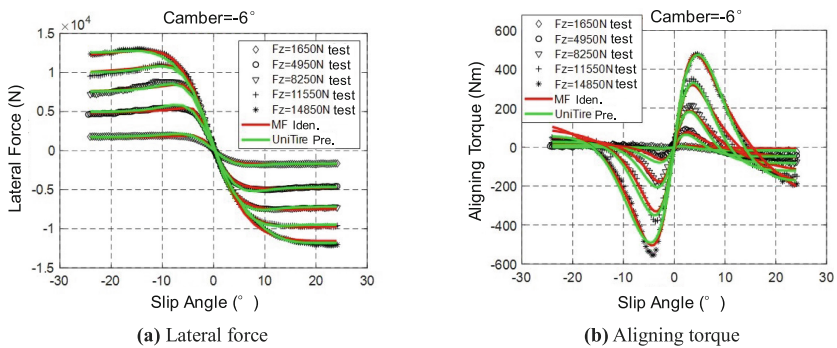(a) Lateral force   (b) Aligning torque

Fig. 13. Prediction result of UniTire.

5 Conclusion

A method for obtaining tire camber-sideslip combined mechanical characteristics based on pure camber and pure sideslip is developed. The prediction method is divided into three parts: the cornering stiffness, the transition zone and the friction. The cornering stiffness prediction is based on the load transferring along tire width caused by camber.

In this way, the cornering stiffness prediction only needs pure sideslip results. The transition zone mechanical characteristics is predicted by treating camber as a function of load. The equivalent load considering camber function is used in both lateral force and pneumatic trail calculation. By verifying the equivalence of camber and slip angle based on LLC, the camber is treated as a function of slip angle in friction prediction. The application verifications of the prediction method in MF and UniTire shows high accuracy. Compared with conventional simulation, the use of prediction method can help with the short cycle development in vehicle virtual prototyping.

References

1. Ahlert, A.: The future of vehicle development using virtual prototypes and an interconnected software infrastructure. In: 22 Internationales Stuttgarter Symposium: Automobil-und Motorentechnik. Wiesbaden: Springer Fachmedien Wiesbaden, 229–243 (2022)
2. Du, H., Jiang, Q., Ruan, Y., et al.: Motion simulation of electric tracked vehicle based on virtual reality fusion. In: 2022 8th International Conference on Virtual Reality (ICVR). IEEE, 163–167 (2022)
3. Cao, D., Wang, X., Li, L., et al.: Future directions of intelligent vehicles: potentials, possibilities, and perspectives. IEEE Trans. Int. Veh. **7**(1), 7–10 (2022)
4. Calabrese, F., Bäcker, M., Gallrein, A., et al.: Virtual tire design/assessment in the early vehicle development process. In: The IAVSD International Symposium on Dynamics of Vehicles on Roads and Tracks. Springer, Cham, 1350–1359 (2019)
5. Lugaro, C., Niedermeier, F., Wassertheurer, B., et al.: Method for virtual tyre and braking distance simulation. ATZ Worldwide (2017)
6. Na, J., Gil, G.: Virtual optimization of tire cornering characteristics to satisfy handling performance of a vehicle. SAE Technical Paper (2016)
7. VI-grade. VI-grade VIC2020 | Goodyear | Virtual is Becoming Reality in the Tire Industry [Video file]. (2020–07–15) [2022–07–23]. https://www.youtube.com/watch?v=RNQG6DtAepQ
8. Bansal, V., Goyal, S., Nair, A., et al.: Improvement in FEA prediction of tire performance by incorporating variable friction between tire and road, Constitutive Models for Rubber XI. CRC Press 458–463 (2019)
9. ABAQUS/Standard User's Manual, Version 6.9. / Smith, Michael
10. https://calspan.com/automotive/tire-performance-testing. Retrieved Jan. 1, 2024
11. Pacejka, H.: Tire and vehicle dynamics Ed. 3. Elsevier Science, 2012
12. Dang, L.: Modeling and experimental study of tire camber mechanical characteristics. (Doctoral dissertation, Jilin University)
13. Velenis, E., Tsiotras, P., Canudas-De-Wit, C., et al.: Dynamic tyre friction models for combined longitudinal and lateral vehicle motion. Veh. Syst. Dyn. **43**(1), 3–29 (2005)
14. Lu D, Wang D, Wang C, et al.: Tire carcass camber and its application for overturning moment modeling. SAE Technical Paper (2013)
15. Guo, K., Lu, D.: UniTire: unified tire model for vehicle dynamic simulation. Veh. Syst. Dyn. **45**(S1), 79–99 (2007). https://doi.org/10.1080/00423110701816742